Article:

Rigby, S.E., Akintaro, O.I., Fuller, B.J. et al. (4 more authors) (2019) Predicting the response of plates subjected to near-field explosions using an energy equivalent impulse. International Journal of Impact Engineering, 128. pp. 24-36. ISSN 0734-743X

https://doi.org/10.1016/j.ijimpeng.2019.01.014

Predicting the response of plates subjected to near-field explosions using an energy equivalent impulse

S.E. Rigby[a,*], O.I. Akintaro[a], B.J. Fuller[a], A. Tyas[a,b], R.J. Curry[c], G.S. Langdon[c], D.J. Pope[d]

[a] *Department of Civil & Structural Engineering, University of Sheffield, Mappin Street, Sheffield, S1 3JD, UK*
[b] *Blastech Ltd., The BioIncubator, 40 Leavygreave Road, Sheffield, S3 7RD, UK*
[c] *BISRU, Department of Mechanical Engineering, University of Cape Town, Rondebosch 7700, Republic of South Africa*
[d] *Defence Science and Technology Laboratory (Dstl), Porton Down, Salisbury, Wiltshire, SP4 0JQ, UK.*

Abstract

Recent experimental work by the current authors has provided highly spatially and temporally resolved measurements of the loading imparted to, and the subsequent dynamic response of, structures subjected to near-field explosive loading [1]. In this article we validate finite element models of plates subjected to near-field blast loads and perform a parametric study into the relationship between imparted load and peak and residual plate deformation. The energy equivalent impulse is derived, based on the theory of upper bound kinetic energy uptake introduced herein, which accounts for the additional energy imparted to a structure from a spatially non-uniform blast load. Whilst plate deflection is weakly correlated to *total* impulse, there is shown to be a strong positive correlation between deflection and *energy equivalent* impulse. The strength of this correlation is insensitive to loading distribution and mode of response. The method developed in this article has clear applications for the generation of fast-running engineering tools for the prediction of structural response to near-field explosions.

Keywords: Blast loading, Deformation, Energy equivalent impulse, Finite element analysis, Plates

1. Introduction

The provision of adequate blast protection systems requires a detailed understanding of the magnitude and distribution of the imparted load, and the response of a structure subjected to this load. The blast protection community is equipped with well-established engineering tools, such as the Kingery and Bulmash semi-empirical method [2] which allows for rapid evaluation of blast wave parameters from a given explosive event, and the equivalent single-degree-of-freedom method [3] which can be used to calculate the response of idealised structures subjected to dynamic loads. Such engineering tools have been demonstrated to be accurate for geometrically simple scenarios (e.g. [4, 5]), however these methods are unsuitable when considering the highly complex, spatially non-uniform

*Tel: +44 (0) 114 222 5725
Email address: sam.rigby@shef.ac.uk (S.E. Rigby)

loading conditions that arise from the detonation of an explosive located extremely close to a structure. This 'near-field' blast issue is of considerable importance, in issues ranging from protection against the effects of land-mines and small improvised explosive devices, to the design and evaluation of explosive storage facilities or critical infrastructure. There is a pressing need for approaches which combine fundamental understanding of the qualitative mechanisms of loading and structural response with the ability to quantitatively predict these effects, leading to simple, but well-founded quick-running engineering models which can be used in risk assessment studies.

Explicit finite element software can be used to model the detonation process, blast wave propagation and subsequent target response through fluid-structure interaction. Whilst this method can often produce results that are in excellent agreement with experimental observations [6, 7, 8, 9, 10, 11], the high computational cost associated with these analyses often limit the suitability of this approach for practical engineering decision-making. Furthermore, such numerical work is often conducted in the absence of detailed, well-controlled experimental data on blast loads and target deformation.

An alternative method is to apply the load directly to the target using pre-defined point loads, taken from numerical model results, experimental recordings, or semi-analytical predictions [12, 13, 14, 15, 16]. Whilst this may result in significant computational savings by negating the need to account for analyses involving fluid-structure interaction, the accuracy of such models is highly dependent on the validity of the load model itself and existing models are unproven in near-field blast load scenarios.

Previous work at the Blast Impact and Survivability Research Unit (BISRU) at the University of Cape Town (UCT), South Africa, into plate response from uniform impulsive loads has shown that a linear relationship exists between impulse and residual deflection [17, 18]. Whilst more recent studies into plate deformation under non-uniform blast loads have shown that a similar relationship can be derived if the distribution of loading is *assumed* [19, 20, 21, 22], there have, to date, been no studies where the loading distribution is *known*.

The current authors have previously presented the results from a dual experimental programme conducted at the University of Sheffield (UoS), UK, and BISRU at UCT [1]. UoS tests were performed using the Characterisation of Blast Loading (CoBL) apparatus [23] to capture the spatial and temporal distribution of pressure and specific impulse resulting from the detonation of near-field free-air explosions. UCT tests were performed using a blast pendulum, recently modified to include stereo high speed video (HSV) capabilities [24]. Digital Image Correlation (DIC) [25] was used to measure the transient deformation along the centreline of blast loaded circular plates.

This paper presents a study into the specific impulse distribution, kinetic energy uptake, and resultant transient plate deformation arising from the interaction of a near-field explosive detonation with a target plate, using results from Ref. [1] to validate the following numerical modelling approaches:

- Free-air blast load validation in an axi-symmetric Multi-Material Arbitrary Lagrangian-Eulerian (MMALE) simulation
- Dynamic plate deformation using MMALE method
- Dynamic plate deformation using Lagrangian method

Initially the UoS experiments are simulated using an axi-symmetric model, and the resulting pressure and specific impulse distributions are compared to the experimentally measured values. Subsequently, 3D quarter-symmetric models of the UCT target plates are simulated using both a MMALE and Lagrangian formulations, and transient deformations are compared to the experiments. In the Lagrangian models, scaled UoS impulse distributions are applied directly to the plates as equivalent initial velocities, whereas in the MMALE models the explosion process is explicitly simulated and pressure loads are transferred to the structure through fluid-structure coupling.

Finally, the *energy equivalent* uniform impulse load is derived, and a parametric study is conducted which investigates the relationship between plate deformation and energy equivalent impulse.

2. Free-air blast load validation

Prior to simulating the plate deformation experiments, a free-air blast validation exercise was performed using the LS-DYNA explicit solver (LSDYNA V971 R8.10) developed by Livermore Software Technology Corporation [26]. Reflected pressure and impulse acting on a rigid target were directly measured in high explosive tests conducted at the University of Sheffield [1], and serve as validation data in this section. Seven tests were conducted in total: three tests were performed using 100 g PE4 spheres detonated at 55.4 mm clear stand-off distance (SOD) from the target, and four tests were performed using 78 g PE4 cylinders with diameter:height ratio of 3:1 detonated at 168.0 mm clear SOD. Temporal features of the loading and spatial distributions are compared against LS-DYNA results.

The Multi-Material Arbitrary Lagrangian-Eulerian (MMALE) solver and van Leer half-index shift [27] advection algorithm were specified. This enabled the air and explosive to be modelled as two distinct parts, with a full description of the air and the explosive given below.

2.1. Geometric representation

A 250×250 mm rectangular domain of 1 mm square axi-symmetric shell elements was used for both spherical and cylindrical charge configurations. The *y*-axis represented the axis of symmetry, and the top edge of the domain was constrained against normal translations to act as a rigid boundary. The two remaining domain edges were set as non-reflecting boundaries to allow the blast wave to freely propagate out of the domain. A preliminary mesh sensitivity study indicated that a 1 mm mesh was adequate to achieve impulse convergence, and that an increase or decrease in the default bulk viscosity parameters had little effect on the fidelity or accuracy of the results.

All elements in the domain were initially assigned as air, and the *INITIAL_VOLUME_FRACTION_GEOMETRY keyword was used to ‘fill’ the explosive volume. For the spherical charge validation, container type 6 (sphere) was selected, and a 24.6 mm radius sphere – centred on the axis of symmetry and 80 mm from the reflecting boundary – was specified. For the cylindrical charge validation, container type 5 (rectangular box) was selected, with one corner located on the axis of symmetry and 168 mm from the reflecting boundary, and the other corner located 28.6 mm from the axis of symmetry and 187 mm from the reflecting boundary. These geometries directly correspond to the UoS experimental setup detailed in Ref. [1], given a density of 1601 kg/m^3 for PE4, and are shown in Figure 1.

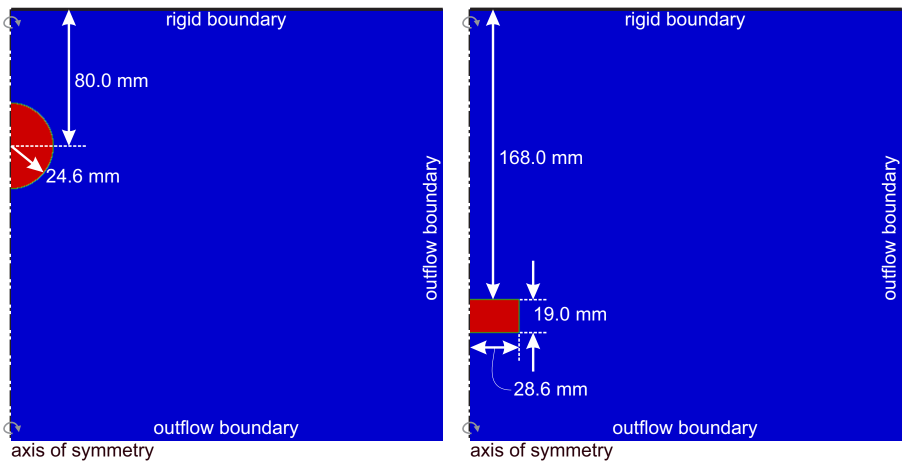

Figure 1: Geometry of the spherical [left] and cylindrical [right] blast load validation models

2.2. Material properties and equations of state

The air was modelled using the MAT_NULL material model and EOS_LINEAR_POLYNOMIAL equation of state (EOS), an arbitrary polynomial expression describing the relationship between pressure, density, and energy. The EOS_LINEAR_POLYNOMIAL is given as:

$$p = C_0 + C_1\mu + C_2\mu^2 + C_3\mu^3 + (C_4 + C_5\mu + C_6\mu^2)E \tag{1}$$

where $C_0, C_1, C_2, C_3, C_4, C_5, C_6$ are constants, $\mu = \rho/\rho_0 - 1$, ρ and ρ_0 are the current and initial densities of air, and E is the specific internal energy. If the variables C_0, C_1, C_2, C_3 and C_6 are all set equal to 0, and C_4 and C_5 are set equal to $\gamma - 1$, i.e. 0.4, where γ is the ratio of specific heats ($\gamma = 1.4$ for air), the ideal gas equation of state is recovered:

$$p = (\gamma - 1)E\rho/\rho_0 \tag{2}$$

An initial specific internal energy, $E_0 = 253.4$ kPa, was used to set the atmospheric pressure to 101.36 kPa.

The explosive was modelled using the MAT_HIGH_EXPLOSIVE_BURN material model and Jones-Wilkins-Lee (JWL) semi-empirical equation of state, EOS_JWL [28]. The density, ρ, detonation velocity, D, and Chapman-Jouguet pressure, P_{CJ}, of the explosive are defined in the material model and control the programmed detonation of the explosive [29]. The relationship between pressure, volume, and energy of the post-detonation explosive products is given by the JWL EOS as

$$p = A\left(1 - \frac{\omega}{R_1 V}\right)e^{-R_1 V} + B\left(1 - \frac{\omega}{R_2 V}\right)e^{-R_2 V} + \frac{\omega E}{V} \tag{3}$$

where A, B, R_1, R_2 and ω are constants, V is the volume and E is the specific internal energy as before.

The material properties and EOS parameters for air and PE4 are given in Table 1. As PE4 is nominally identical to C4 [30], EOS parameters used in this study were taken as the C4 parameters published by Dobratz & Crawford [31].

*MAT_NULL

Parameter	Value	Unit
ρ_0	1.225	kg/m^3

*MAT_HIGH_EXPLOSIVE_BURN

Parameter	Value	Unit
ρ_0	1601	kg/m^3
D	8193	m/s
P_{CJ}	28.00E9	Pa

*EOS_LINEAR_POLYNOMIAL

Parameter	Value	Unit
C_0	0.0	Pa
C_1	0.0	Pa
C_2	0.0	Pa
C_3	0.0	Pa
C_4	0.4	–
C_5	0.4	–
C_6	0.0	–
E_0	253.40E3	Pa

*EOS_JWL

Parameter	Value	Unit
A	609.77E9	Pa
B	12.95E9	Pa
R_1	4.50	–
R_2	1.40	–
ω	0.25	–
E_0	9.00E9	Pa

Table 1: Material model and equation of state parameters for air and PE4 [31]

2.3. Results and discussion

Pressure results were output at 1 mm intervals along the rigid target surface using the *DATABASE_TRACER keyword. Ambient pressure (101.36 kPa) was subtracted from the results to give values in terms of overpressure, and cumulative trapezoidal numerical integration was used to determine impulse histories from the data.

Figure 2 shows numerical and experimental pressure-time and specific impulse-time histories following the detonation of a 100 g PE4 sphere at 55.4 mm clear SOD from a rigid target. Numerical results are provided at 0, 25, 50, 75, and 100 mm from the target centre and are compared with experimental data from Test 1 in Ref. [1]. Figure 3 shows numerical and experimental pressure-time and specific impulse-time histories following the detonation of a 78 g PE4 3:1 cylinder at 168.0 mm clear SOD. Again, numerical results are given at 0, 25, 50, 75, and 100 mm radial ordinate and compared here with experimental data from Test 5 in Ref. [1].

Numerical and experimental peak specific impulse distributions, between 0–100 mm from the target centre, are shown for spherical charges in Figure 4a), and for cylindrical charges in Figure 4b). The experimental results for the spherical tests comprise three individual experiments with four Hopkinson pressure bars (HPBs) recording at each radial ordinate per experiment (twelve data points per radial ordinate), with the exception of the 0 mm radial ordinate where only one HPB per test was used (three data points at 0 mm). The experimental results for the cylindrical tests comprise four individual experiments, again with four HPBs per radial ordinate per test (sixteen

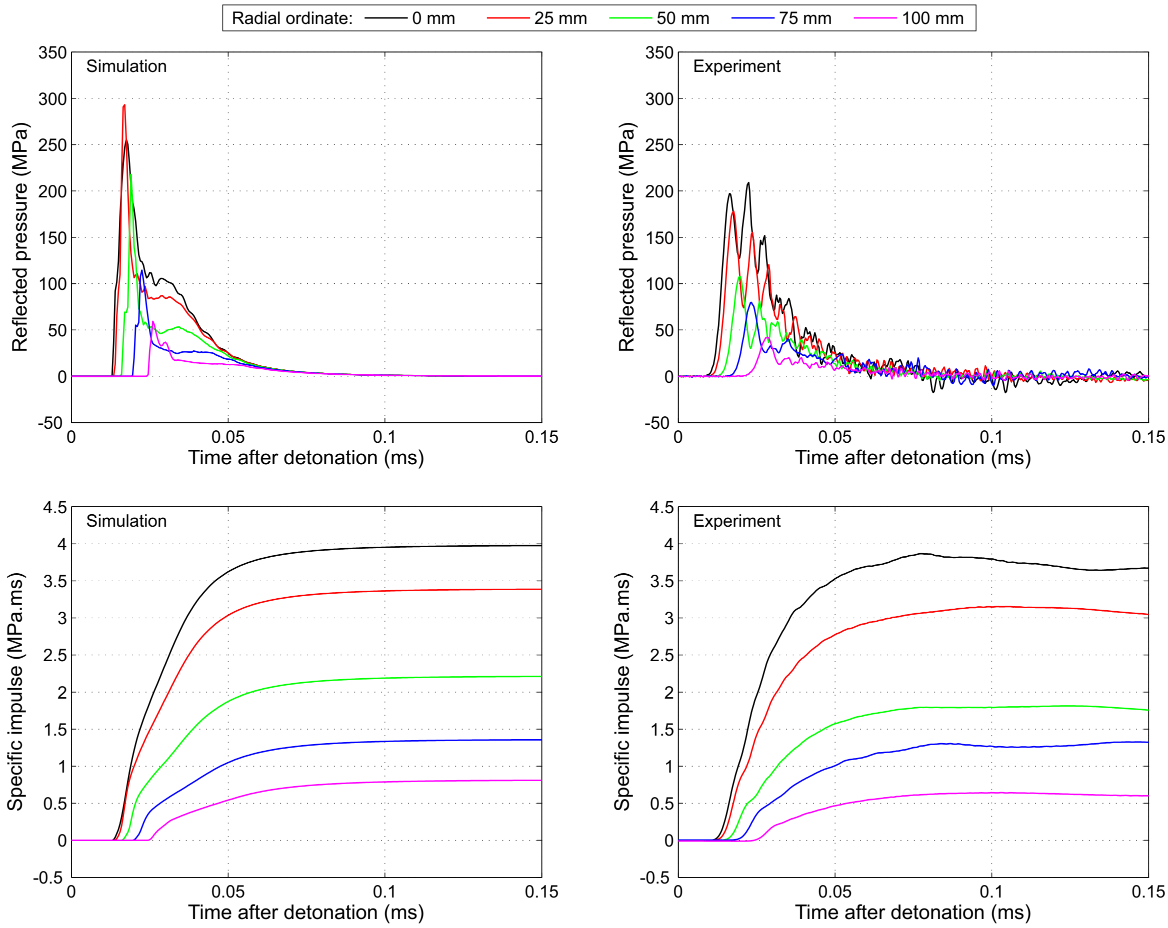

Figure 2: Numerical pressure-time and specific impulse-time histories (100 g PE4 sphere at 55.4 mm clear stand-off distance) compared with data from Test 1 in Ref. [1]

data points per radial ordinate) with the exception of the central bar (four data points at 0 mm). Further details of the experimental setup are available in Part I [1]. Presenting the dataset as a whole, as opposed to a mean distribution, gives an indication of typical upper and lower bounds on the experimental data and facilitates comparison with the numerical model. The numerical specific distributions are taken directly from temporal integration of the pressure histories extracted from the model – at 1 mm spacing along the rigid boundary – and have not been curve-fitted or processed any further.

Qualitatively, the general form of the spherical pressure-time and specific impulse-time histories (Figure 2) appear to be in good agreement, despite the experimental signals exhibiting some Pochhammer-Chree dispersion

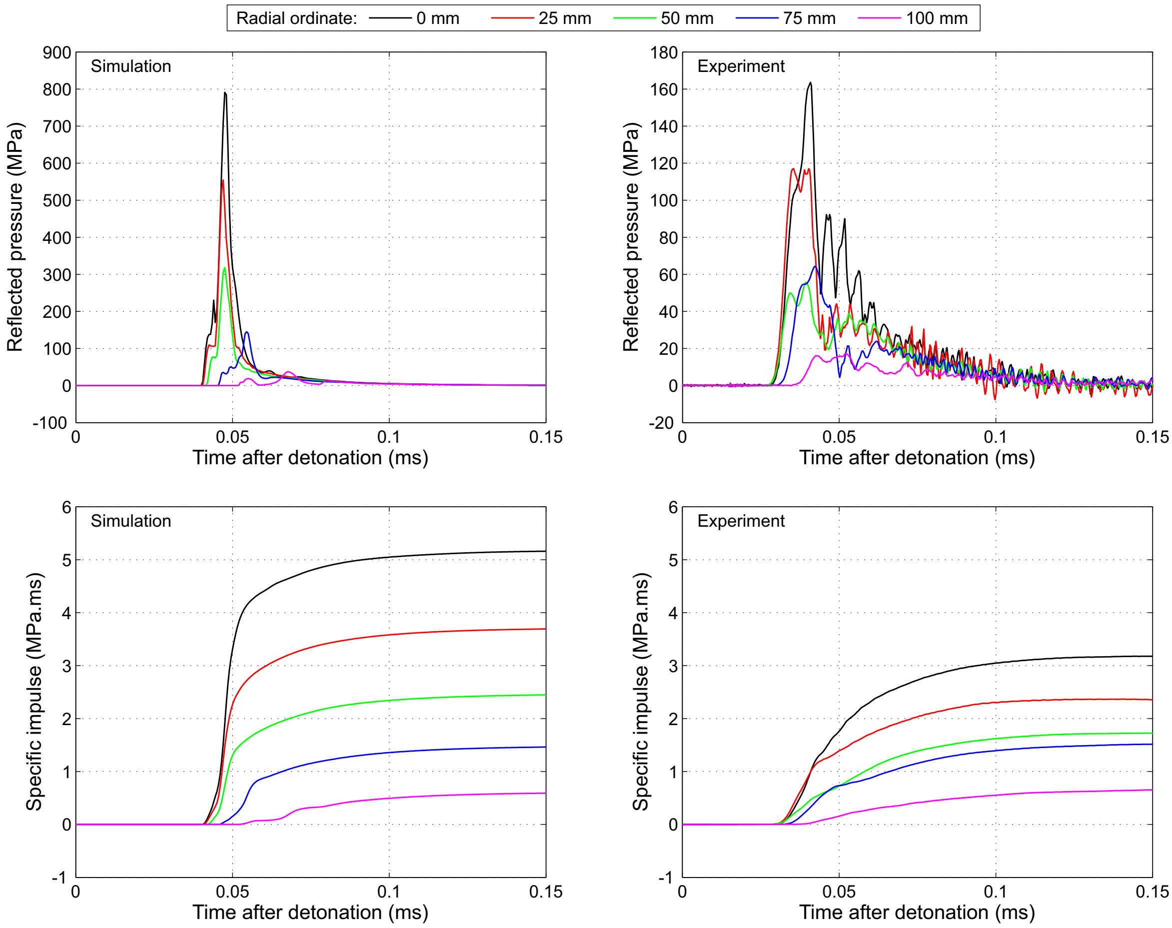

Figure 3: Numerical pressure-time and specific impulse-time histories (78 g PE4 3:1 cylinder at 168.0 mm clear stand-off distance) compared with data from Test 5 in Ref. [1]

effects [32]. This can be seen as a loss of definition of transient pressure features of durations <~4 microseconds (for the current bar diameter [33]) and the presence of spurious oscillations following the head of the pulse. Accordingly, it is inappropriate to compare peak pressures, however Pochhammer-Chree dispersion does not affect total impulse, and only marginally affects the temporal evolution of impulse. It can be seen that temporal development of the impulses (Figure 2), and peak impulse distributions (Figure 4a) are well captured by the numerical model for the spherical charges. The experimental and numerical arrival times also compare well.

In contrast, the cylindrical experimental and numerical results compare less well. The peak pressures acting at locations between 0–50 mm from the plate centre are approximately five times greater than the experimentally

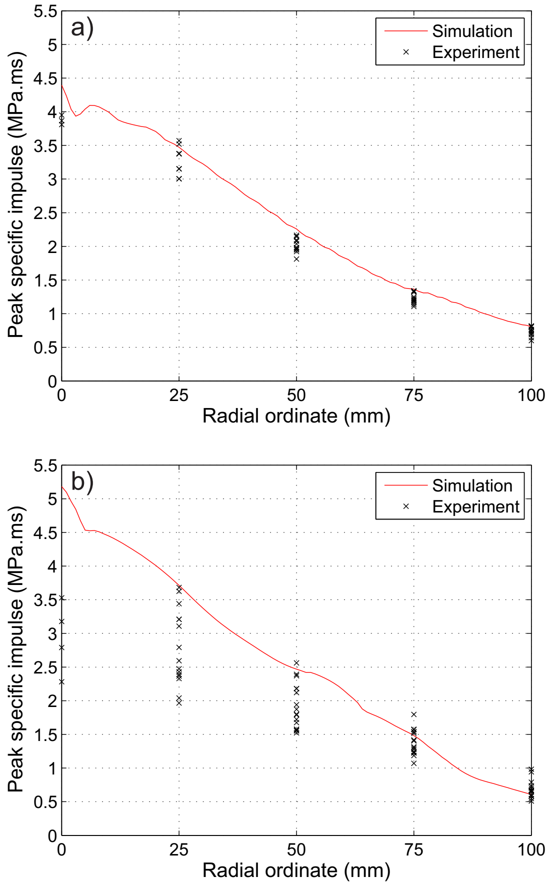

Figure 4: Numerical and experimental peak specific impulse distributions: a) 100 g sphere at 55.4 mm clear stand-off distance; b) 78 g 3:1 cylinder at 168.0 mm clear stand-off distance

recorded values (note the vertical axis values), and numerical positive phase durations are considerably lower than in the experiments (Figure 3). The numerical and experimental cylindrical specific impulse distributions (Figure 4b) appear to converge at ~75 mm from the target centre, however closer to the centre the numerical model considerably over-predicts specific impulse. This over-prediction, however, may not have a significant influence on plate deformation owing to the relatively small area of the plate that it acts over.

In summary, the validation exercise has demonstrated that LS-DYNA can simulate the impulse distribution from near-field blast waves to a reasonable degree of accuracy, particularly when considering the spatial distribution of peak specific impulse.

3. Plate deformation model set up

Plate deformations were simulated using two distinct methods:

- 3D quarter-symmetric MMALE model, with detonation and blast wave propagation modelled directly and loading applied to the plate through fluid-structure-interaction
- 3D quarter-symmetric Lagrangian model, with loading directly applied to each node as an initial velocity

Each model was analysed under two loading conditions, namely from spherical and cylindrical explosive charges. In the experiments conducted at UCT, described in [1], 300 mm diameter, 3 mm thick Domex 355MC steel plates, fully clamped along the periphery (all displacements and rotations nominally constrained) were subjected to spherical and cylindrical near-field blasts. The test geometries were designed using Hopkinson-Cranz scaling [34, 35] to ensure the scaled distance and scaled geometry were the same as those in the UoS tests for each charge shape. Ten tests were conducted at UCT in total: five using 50 g spheres at 44.0 mm clear distance (63.5 mm to charge centre), and five using 50 g 3:1 (diameter:height) cylinders at 145.0 mm clear distance (153.3 mm to charge centre), and are used herein as validation data.

3.1. Geometric representation

The plates, clamp frames, and air domain and explosive (in the MMALE models only) were modelled in 3D quarter-symmetry, as can be seen in Figure 5. In both MMALE and Lagrangian models the plates were meshed with 2×2 mm, 4-noded fully integrated quadrilateral shell elements with 3 mm thickness and five through-thickness integration points, and a quarter of the plate (200×200 mm square) was modelled. The clamp frames were meshed with 8-noded tetrahedral solid elements with a typical side length of 4 mm, and were separated from the plate elements by ±1.5 mm to account for the plate thickness.

In the spherical charge MMALE models, the plate and clamp frames were situated within a 200×200×200 mm air domain comprising 8-noded brick elements, again with 2 mm side length. Element sizes for all parts were based on the results from a previous mesh sensitivity study [36]. The domain was extended to 200 × 200 × 300 mm for the cylindrical charge MMALE model to account for the larger SOD. The air domains were over-sized by approximately 50 mm past the target plates to allow for fluid-structure interaction to be maintained whilst the plates were deforming. In both MMALE models, the explosive was again represented using the

*INITIAL_VOLUME_FRACTION_GEOMETRY keyword. As with the axi-symmetric models, the 3D spherical charges were represented using container type 6 (sphere) with a 19.5 mm radius specified – centred on the x and y axes, 63.5 mm from the plate surface. The 3D cylindrical charges were represented using container type 4 (conical surface), with 16.5 mm height and 24.5 mm top and bottom radii, centred on the x and y axes, 153.3 mm from the plate surface.

Boundary conditions were imposed on all parts to enforce xz and yz symmetry conditions. All other surfaces of the air part were defined as free boundaries to permit flow out of the air domain. An additional rigid boundary condition was imposed on the rear clamp frame to represent the area where the clamp frame was mounted to the pendulum (the movement of the pendulum within the duration of loading was assumed to be negligible).

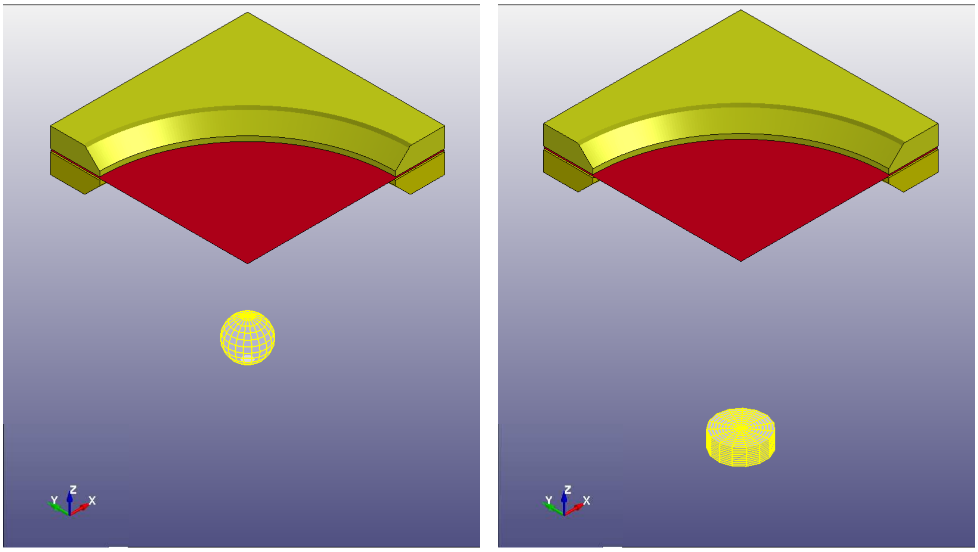

Figure 5: Quarter-symmetric representation of the spherical [left] and cylindrical [right] plate deformation models (note: explosive geometries are shown in their full 3D representation for clarity)

3.2. *Plate and clamp frame material properties*

In the MMALE models, the air and PE4 were modelled using the same material properties and equations of state as described above in the axi-symmetric load validation study (see Table 1). The 3 mm Domex 355MC steel plates were represented using the simplified Johnson-Cook material model, which relates the equivalent stress, σ_{eq} to the equivalent strain, ϵ_{eq}, and equivalent strain rate $\dot{\epsilon}_{eq}$ [37],

$$\sigma_{eq} = \left[A + B{\epsilon_{eq}}^{n}\right]\left[1 + C\ln\frac{\dot{\epsilon}_{eq}}{\dot{\epsilon}_0}\right] \tag{4}$$

where A, B, n, and C are material constants. Thermal softening effects and damage are ignored in the simplified Johnson-Cook material model. No failure criterion was specified as the plates were not loaded to failure in the experiments. Johnson-Cook material parameters for the Domex 355MC steel plates were determined by Curry [38] using LS-OPT [39], a standalone optimisation package which interfaces with LS-DYNA. Static (A, B, n) material properties were calibrated using LS-OPT by minimising the error between numerical and experimental force-displacement curves determined from static tensile tests. Subsequently, the error between numerical and experimental force-displacement curves, determined from dynamic split-Hopkinson bar experiments, was minimised in order to determine the dynamic material parameter, C. Johnson-Cook material properties are shown in Table 2, where ρ, E, and ν are density, Young's Modulus, and Poisson's ratio.

*MAT_SIMPLIFIED_JOHNSON_COOK

Parameter	Value	Unit
ρ	7830	kg/m^3
E	206.8E9	Pa
ν	0.3	–
A	362E6	Pa
B	642E6	Pa
n	0.5597	–
C	0.032	–

Table 2: Johnson-Cook material properties for Domex 355MC steel

The clamp frames were modelled as linear elastic with ρ=7850 kg/m^3, E=205 GPa, and ν=0.29, as negligible deflections were expected to occur within the frame itself.

3.3. Contact and fluid-structure coupling

Coupling between the plate and clamp frames was achieved using automatic surface-to-surface penalty contact. A coefficient of static friction of $\mu_s = 0.17$ was assigned to model the friction between the two surfaces, after Geretto [36]. The bolted connections between the plate and clamp frames were represented by linear spring elements, with spring stiffness and initial elongation specified to achieve an equivalent pre-stress of 240 MPa in the bolts. This method simplifies the modelling of the clamping force between the plate, and is an acceptable approach given that no noticeable pull-in or tearing was observed at the boundary during the experiments. Fluid-structure coupling in the MMALE models was achieved using the *CONSTRAINED_LAGRANGE_IN_SOLID keyword with compression penalty contact specified between the plate and a part set containing the air and explosive.

3.4. Representation of loading in Lagrangian model

The applied load in the Lagrangian models was created using a bespoke MatLab script which imported the plate mesh and assigned each node with an initial velocity based on its position using the *INITIAL_VELOCITY_NODE keyword. As an imparted impulse results in an equivalent change in momentum, the initial velocity, v, at a distance x from the plate centre is given as

$$v(x) = \frac{i(x)}{\rho t} \tag{5}$$

where i is specific impulse, and ρ and t are density and thickness of the plate, 7830 kg/m^3 and 3.00 mm respectively. This approach has been used previously to assign impulsive loads in LS-DYNA [16, 40].

Specific impulse distributions were directly measured for 100 g PE4 spheres and 78 g PE4 cylinders at UoS [1]. A spline interpolant was fitted to the data, passing through the mean value of all recordings at 0, 25, 50, 75 and 100 mm for each charge configuration. The following conditions were applied to the spline interpolant: zero gradient at the plate centre; zero gradient and zero impulse at an arbitrary large radial offset from the plate centre; and non-negative peak specific impulse at any radial ordinate. These conditions ensured the spline interpolant was physically valid, i.e. radially symmetrical and monotonically decreasing with increasing distance from the plate centre [1]. The fitted specific impulse distributions from the UoS tests are shown in Figure 6.

Given that the plate deformation tests at UCT, detailed in Ref. [1], used 50 g PE4 spheres and cylinders, Hopkinson-Cranz scaling [34, 35] has been used to express the UoS-recorded specific impulse distributions at UCT scale, i.e. specific impulses and distances (stand-off and radial ordinate) are divided by the cube-root of the relative charge masses: $\sqrt[3]{100/50} = 1.26$ for the spherical tests and $\sqrt[3]{78/50} = 1.16$ for the cylindrical tests respectively. The fitted distributions expressed at UCT scale are also shown in Figure 6.

3.5. Simulation phases

The MMALE models were run in three phases:

1. Loading phase (0–0.5 ms)
2. Deformation phase (0.5–10 ms)
3. Damping phase (10–20 ms)

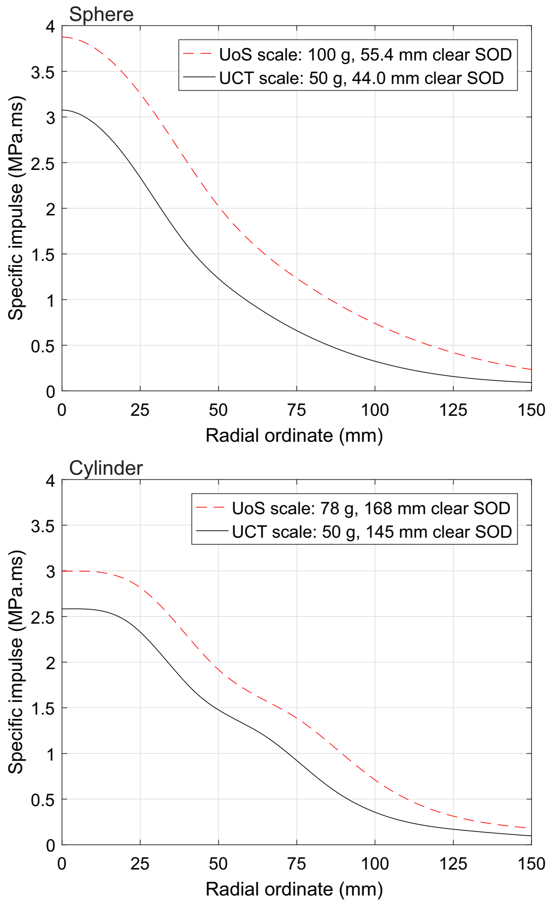

Figure 6: Specific impulse distributions from Ref. [1] for spherical and cylindrical explosive charges, expressed at UoS and UCT scales

In Phase 1, the loading was applied to the plate through fluid-structure coupling, following direct simulation of the detonation process, blast wave propagation, and target interaction. After 0.5 ms, the blast pressure was judged to have reached ambient (or near-ambient) conditions across the plate and the simulation was terminated. Phase 2 was initiated using a 'small restart' file in LS-DYNA, where the air and explosive parts were deleted, fluid-structure coupling was removed, and the plate was free to deform and interact with the clamping frame. After 10 ms, the analysis was again terminated, and Phase 3 was initiated with a small restart file with added structural damping to allow the plate to reach its residual deflection profile.

The Lagrangian models were run in two phases, since the loading was applied as an initial condition and, according to impulsive loading conditions, the 'loading phase' has zero duration:

1. Deformation phase (0–10 ms)
2. Damping phase (10–20 ms)

4. Plate deformation results

4.1. Transient plate deformations

Figure 7 shows experimental midpoint plate deflections [1], measured using digital image correlation, compared with results from MMALE and Lagrangian numerical models for 3 mm thick, 300 mm circular spanning Domex 355MC steel plates subjected to the blast load from a 50 g PE4 sphere at 44.0 mm clear SOD. Figure 8 shows experimental and numerical midpoint plate deflections for 3 mm thick, 300 mm circular spanning Domex 355MC steel plates subjected to the blast load from a 50 g PE4 cylinder (3:1 diameter:height) at 145.0 mm clear SOD. The time-base of the Lagrangian models has been shifted to account for the arrival time of the blast waves: the loading was applied as an initial velocity at $t = 0$, which corresponds the time of detonation in the experiments and MMALE models rather than the true time of arrival. Peak midpoint and residual midpoint deflections are summarised in Table 3 for spherical and cylindrical charge configurations. The experimental means are calculated from an average of three tests (peak) and five tests (residual) per charge configuration.

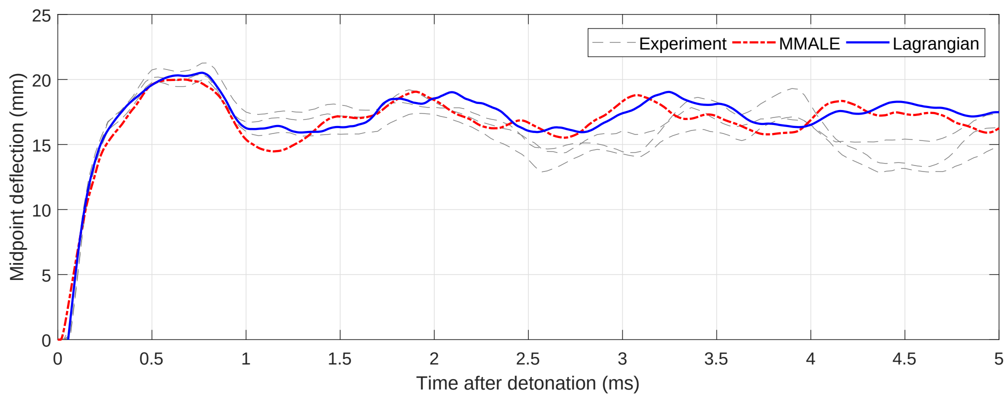

Figure 7: Transient midpoint deflections from experiments [1] and MMALE and Lagrangian numerical models: 50 g PE4 sphere at 44.0 mm clear SOD

The MMALE and Lagrangian models are in excellent agreement with the experimental results, particularly for peak midpoint deflection where both MMALE models are within 2.6% of mean experimental value, and both Lagrangian models are within 0.6% of the mean experimental value. This is a clear indication that, for near-impulsive

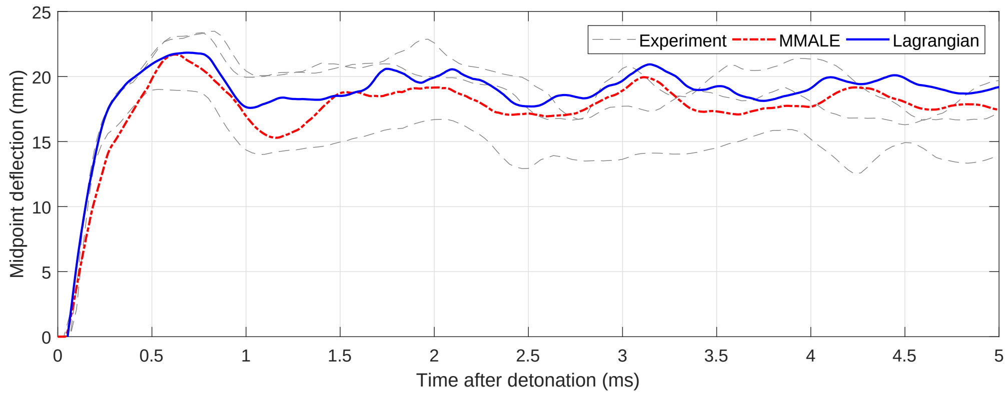

Figure 8: Transient midpoint deflections from experiments [1] and MMALE and Lagrangian numerical models: 50 g PE4 cylinder at 145.0 mm clear SOD

Type	Charge configuration	Peak deflection (mm)	% diff. from experimental mean	Residual deflection (mm)	% diff. from experimental mean
Experiment, mean	Sphere	20.54	–	15.86	–
Experiment, max	Sphere	21.27	3.6	16.31	2.9
Experiment, min	Sphere	19.95	-2.9	15.39	-3.0
MMALE	Sphere	20.00	-2.6	17.19	8.4
Lagrangian	Sphere	20.52	-0.1	17.51	10.4
Experiment, mean	Cylinder	21.96	–	17.91	–
Experiment, max	Cylinder	23.48	6.9	19.17	7.0
Experiment, min	Cylinder	19.01	-13.4	15.29	-14.6
MMALE	Cylinder	21.69	-1.2	18.11	1.1
Lagrangian	Cylinder	21.83	-0.6	19.27	7.6

Table 3: Peak midpoint and residual midpoint deflections from experiments [1] and MMALE and Lagrangian numerical models for spherical and cylindrical charges

loading conditions, the load distribution measured from an experimental test series can be directly mapped onto a finite element model of a plate to accurately predict the transient and resultant deformation. The accuracy of the Lagrangian models is commensurate with the accuracy of the MMALE models, which is particularly noteworthy considering that the MMALE models took ~20 hours in total to run on a desktop PC, whereas the Lagrangian models typically completed in ~2 hours.

The transient behaviour of the plates is well captured in the MMALE and Lagrangian numerical models, as seen in Figures 7 and 8. The Lagrangian models track the experimental displacements near-perfectly for the first few tens of microseconds of displacement, whereas the MMALE models exhibit a more gradual rise. It is suggested that this is due to the rounding of the shock pressures in the MMALE model due to mesh effects, which results in a more gradual application of load. The post-peak behaviour of the plates is well captured in both models, with the presence of higher frequency (vibration period ~0.3 ms) and lower frequency (vibration period ~1.0 ms) modes of vibration apparent in the experimental and numerical deflection histories.

Two observations become apparent: firstly, the numerical models appear to represent the *average* plate behaviour well both in terms of peak deflection and transient behaviour; secondly, the cylindrical data has considerably more spread than the spherical data. It is interesting to note that for the spherical tests, the largest deviation in total applied impulse was 3.5% from the mean, and the largest deviation in peak deflection was 3.6% from than the mean (Table 3 in Ref. [1]). For the cylindrical tests, however, the largest deviation in total applied impulse was 6.0% from the mean, and the largest deviation in peak deflection was 14.6% from the mean (Table 4 in Ref. [1]). This indicates that localised variations in specific impulse have more significant influence on plate deformation than on total impulse. Currently, the MMALE models cannot account for this localised variability in loading. However, a suitable approach for the Lagrangian models (although not performed as part of this work) would be to apply the loading distribution measured from each *individual* test, rather than the averaged values, in order to assess the sensitivity of plate displacements to changes in localised loading.

4.2. Plate deflection profiles

Figure 9 and Figure 10 show plate deformation profiles at select times for the spherical and cylindrical charge configurations respectively. Generally, the early-time behaviour of the Lagrangian models ($t < 0.5$ ms) appear to be in better agreement with the experiments than the MMALE models. In both spherical and cylindrical cases, at the approximate time of maximum displacement ($t = 0.5$ ms) the MMALE models appear to be in better agreement, however the residual plate profiles are again better matched by the Lagrangian models.

These plots provide strong evidence to suggest that the strain energy distribution in the plates, which is dictated by the initial kinetic energy distribution and therefore the initial loading distribution, is better represented in the Lagrangian models. The difference between numerical and experimental applied loading (Figure 4) is not sufficient enough to cause significant differences in peak displacement, but is sufficient enough to cause differences in residual global plate response.

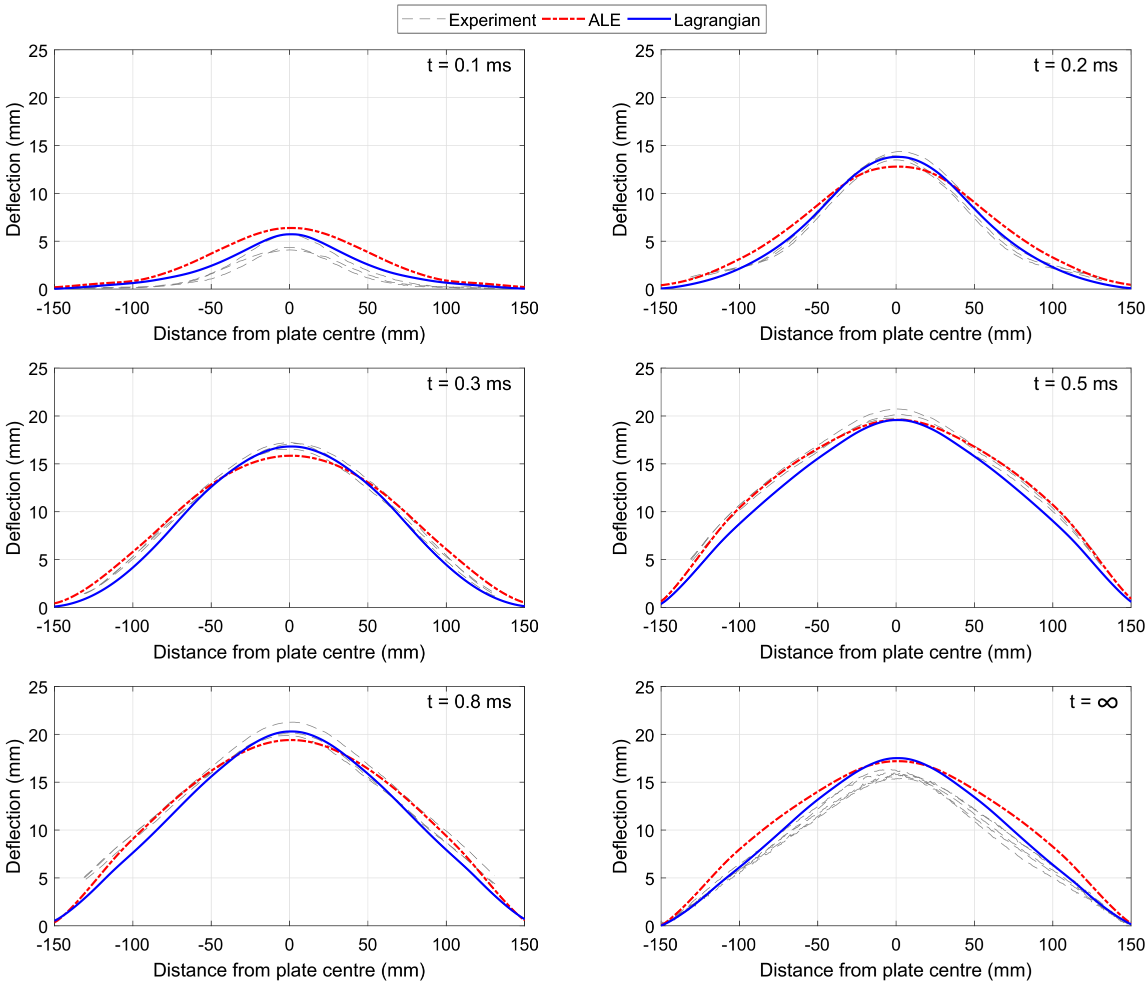

Figure 9: Plate deflection profiles from experiments [1] and MMALE and Lagrangian numerical models: 50 g PE4 sphere at 44.0 mm clear SOD. Transient experimental profiles from DIC, residual experimental profiles ($t = \infty$) from post-test laser scans

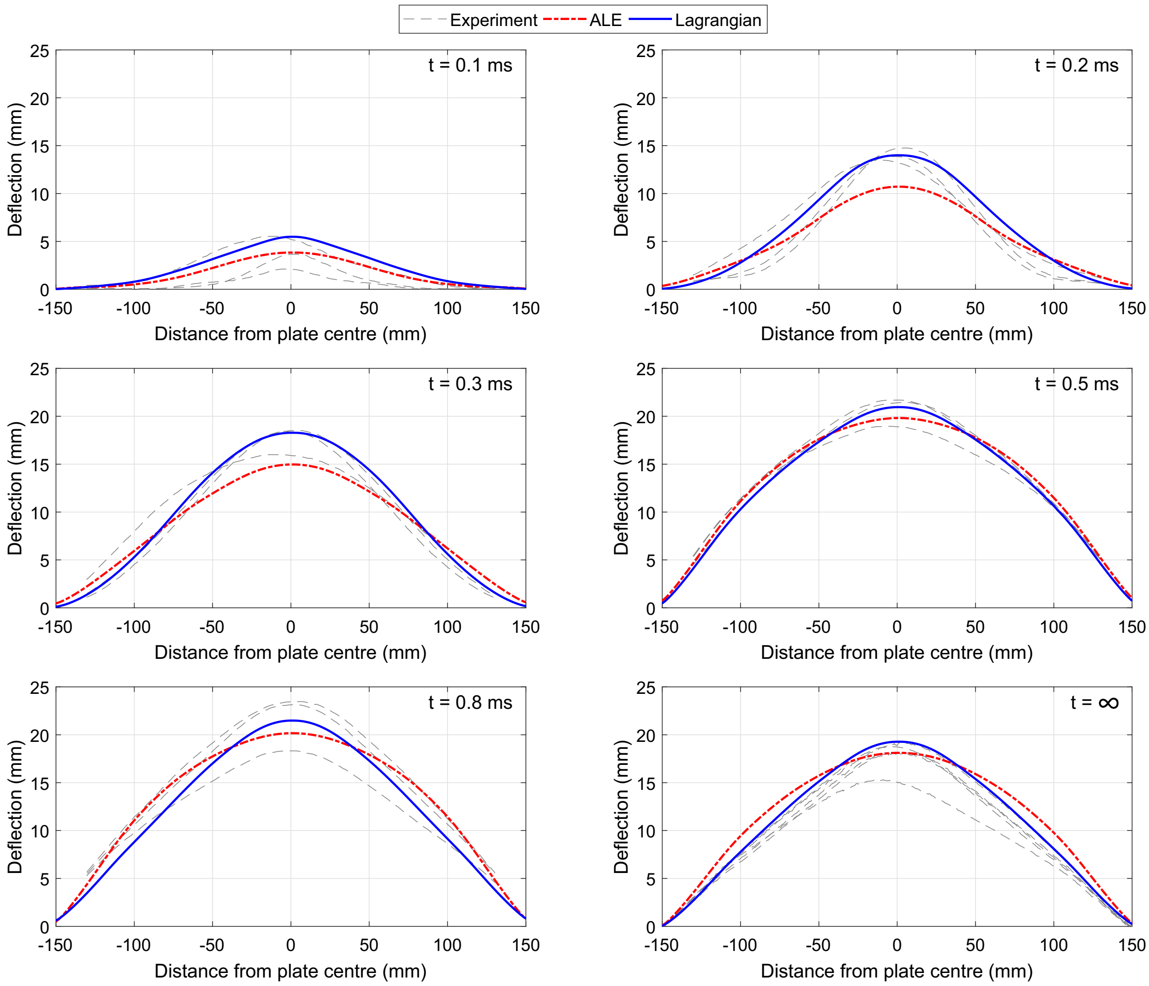

Figure 10: Plate deflection profiles from experiments [1] and MMALE and Lagrangian numerical models: 50 g PE4 cylinder at 145.0 mm clear SOD. Transient experimental profiles from DIC, residual experimental profiles ($t = \infty$) from post-test laser scans

5. Energy equivalent impulse

5.1. Lower bound and upper bound kinetic energy

Under impulsive loading conditions there is zero work done by the imparted load and zero initial internal energy, and hence the entire energy in the system at $t = 0$ is kinetic energy, E_k. Since a change in impulse is equal to a change in momentum, under a uniformly distributed impulsive load the kinetic energy is given as:

$$E_k = \frac{I^2}{2\rho t A} \tag{6}$$

where I is the total impulse acting over the plate, ρ and t are density and plate thickness as introduced previously, and A is the plate area.

Under a non-uniform impulse distribution, as in Figure 11(a), the kinetic energy uptake of the plate is dependent on its deformation profile. Consider the following assumptions:

- A plate behaves as a series of discrete masses
- Each mass is free to move independently of its neighbour
- Each mass is joined to its neighbour by a spring element, which has an arbitrary resistance to shear deformation

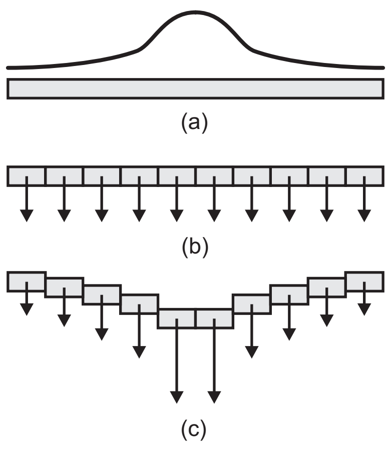

Figure 11: Initial distribution of specific impulse (a), and deformation modes associated with lower bound (b) and upper bound (c) kinetic energy

It follows that the ability of a discrete mass to share load with its neighbours is dependent on the shear resistance of the connecting spring elements. If these elements possess an *infinite* resistance to shear, then each mass would have the ability to instantaneously transfer load to its neighbours and the entire plate would respond as a rigid body, as in Figure 11(b). The velocity profile; kinetic energy uptake of each mass; and hence total kinetic energy, would be a function of the *total impulse acting on the plate* only. Since this response mode assumes infinite shear resistance, it represents a lower bound on the kinetic energy uptake of the plate, $E_{k,l}$. Given that $I = \int_A i \, \mathrm{d}A$, substituting into equation (6) yields:

$$E_{k,l} = \frac{\left(\int_A i \, \mathrm{d}A \right)^2}{2\rho t A} \tag{7}$$

Alternatively, if the masses were connected via elements with *zero* resistance to shear, then the initial velocity profile of the plate would be directly proportional to the impulse distribution, as in Figure 11(c). The kinetic energy of each mass, and therefore the total kinetic energy of the plate, would be dependent on the *distribution of specific impulse acting on the plate*. Since this response mode assumes zero shear resistance, it represents an upper bound on the kinetic energy uptake of the plate, $E_{k,u}$, given as the integral of the kinetic energy of each individual mass:

$$E_{k,u} = \frac{1}{2\rho t} \int_A \frac{(i \, \mathrm{d}A)^2}{\mathrm{d}A} \tag{8}$$

This suggests that, for spatially varying loads, knowledge of total impulse alone is not sufficient to allow for a complete description of the energy uptake of a blast loaded plate. Since the total impulse applied as a uniform load will result in a lower bound estimation of energy uptake (i.e. equation 7 is independent on the distribution of specific impulse), we can define a new term: *energy equivalent impulse*, I_{Ek}. Here, the energy equivalent impulse is defined as a fictitious uniform impulse load that, if applied to a plate, would result in the same energy uptake as the upper bound kinetic energy uptake of the distributed specific impulse load. Since experimental work in Ref. [1] demonstrated that the initial velocity uptake of a plate is directly proportional to the distributed specific impulse, we should expect the upper bound kinetic energy to be a good measure of the actual energy of the system, for thin plates and impulsive loads.

We can also define a factor, K_i, termed the *impulse enhancement factor*, such that

$$I_{Ek} = K_i I. \tag{9}$$

Seeing as impulse is proportional to the square root of kinetic energy (equation 6), we can say that

$$K_i = \frac{I_{Ek}}{I} = \sqrt{\frac{E_{k,u}}{E_{k,l}}} = \sqrt{\frac{\left(\int_A \frac{(i\,\mathrm{d}A)^2}{\mathrm{d}A}\right)A}{I^2}} \tag{10}$$

and therefore

$$I_{Ek} = \sqrt{\left(\int_A \frac{(i\,\mathrm{d}A)^2}{\mathrm{d}A}\right)A} \tag{11}$$

I_{Ek} can be thought of as the *energy*-averaged impulse, as opposed to the *spatially*-averaged impulse, I. The impulse enhancement factor, K_i, is effectively a measure of the uniformity of the distributed load: $K_i = 1$ indicates a perfectly uniform load, and $K_i > 1$ indicates a load that is spatially non-uniform. The greater the value, the greater the difference between upper and lower bound kinetic energies and hence the greater influence of loading non-uniformity on energy uptake.

5.2. Parametric study: setup

A parametric study was undertaken to investigate the influence of loading distribution on the deformation of blast loaded plates. Since the previous modelling in this article has highlighted the accuracy of the spherical Lagrangian model, this was adopted in the parametric study and adapted to account for a range of plate thicknesses and loading magnitudes/distributions. Hopkinson-Cranz scaling was used to modify the applied specific impulse distribution (Figure 6) to model different charge sizes, each detonated at the same scaled distance and acting over a 300 mm circular spanning Domex 355MC steel plate. The distributions used are shown in Figure 12(a), with the respective charge sizes indicated next to each distribution. Figure 12(b) shows the specific impulse distribution and associated average impulse and energy equivalent uniform impulse for the 50 g load curve. Figure 12(c) shows how impulse enhancement factors [left axis] and total impulse [right axis] vary with the charge masses used in the parametric study. As the charge mass increases, the actual stand-off distance increases (for a constant scaled distance), and, as the plates are the same span throughout, the stand-off increases relative to the span and the loading becomes more uniform over the plate surface. Hence, the impulse enhancement factor can be seen to decrease with increasing impulse and increasing charge mass. The input parameters for the parametric study are summarised in Table 4.

Charge mass, W (g PE4)	Plate thickness, t (mm)	Total impulse, I (Ns)	Impulse enhancement factor, K_i (–)	Energy equivalent impulse, I_{Ek} (Ns)
10	0.25–1.00	8.39	2.28	19.11
25	0.50–1.00	19.86	1.77	35.18
50	1.00–5.00	36.97	1.51	55.73
75	1.00–5.00	52.69	1.38	72.85
100	2.00–5.00	67.27	1.31	88.02
150	2.00–5.00	93.57	1.22	114.56
200	2.00–5.00	116.87	1.18	137.71

Table 4: Input parameters used in the parametric study

5.3. Parametric study: results

The results from the parametric study are provided in full in Table 5. In Figure 13, peak deflection (solid line) and residual deflection (dashed line) are plotted against charge mass for the different plate thicknesses studied. It can be seen that each plate thickness forms a distinct grouping with deflections that increase with charge mass and decrease with plate thickness, as is expected.

It has been shown experimentally that there exists a linear relationship between normalised impulse and normalised deflection of plates subjected to uniformly distributed blast loads [17]. Figure 14 shows the deflection results from this parametric study plotted against impulse per unit thickness. Here, the different markers refer to the two different methods for calculating impulse: I is defined as the integral of specific impulse over the plate area, and; I_{Ek} is defined the energy equivalent impulse, i.e. an equivalent uniform impulse that imparts a kinetic energy equal to the upper bound kinetic energy of the distributed load, as introduced in this article.

Linear regressions were fit to the relationships between peak deflection and energy equivalent impulse, and residual deflection and energy equivalent impulse. Both regression lines show a strong positive correlation with an R^2 value of 0.99 in each case. The relationship for peak deflection was set to cross at the origin, whereas the relationship for residual deflection was allowed to cross at a non-zero value to account for elastic strain recovery in the plates.

Charge mass, W (g PE4)	Plate thickness, t (mm)	Peak deflection (mm)	Residual deflection (mm)
10	0.25	79.9	77.8
10	0.50	41.6	41.0
10	1.00	22.9	20.9
25	0.50	72.5	71.9
25	1.00	37.7	36.8
50	1.00	58.1	57.0
50	2.00	30.2	28.5
50	3.00	20.5	17.5
50	4.00	16.0	11.5
50	5.00	12.7	7.2
75	1.00	74.0	72.8
75	2.00	38.8	37.1
75	3.00	25.9	23.6
75	4.00	19.8	16.1
75	5.00	15.9	11.0
100	2.00	45.9	44.2
100	3.00	30.9	28.7
100	4.00	23.2	20.1
100	5.00	18.6	14.5
150	2.00	57.6	55.9
150	3.00	39.1	37.0
150	4.00	29.4	26.7
150	5.00	23.7	20.3
200	2.00	67.3	65.4
200	3.00	45.8	43.6
200	4.00	34.7	32.0
200	5.00	27.9	24.8

Table 5: Plate deflection results from the parametric study

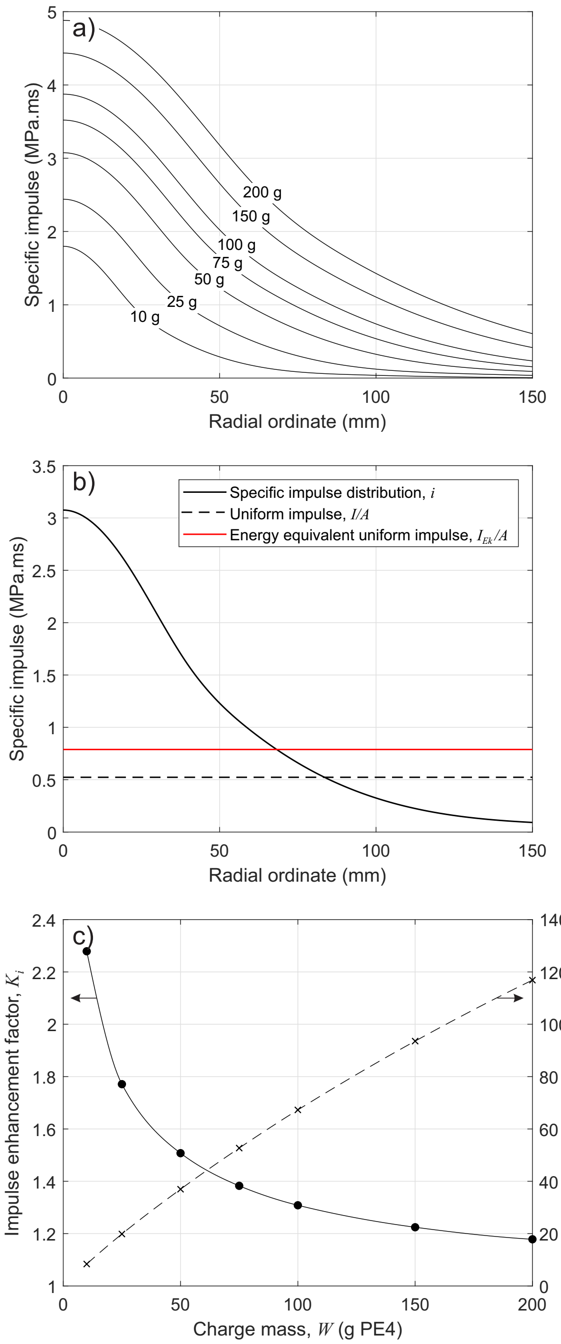

Figure 12: a) Specific impulse distributions used in the parametric study; b) illustration of uniform impulse (I) and energy equivalent uniform impulse (I_{Ek}) for 50 g load case; c) Impulse enhancement factor [left axis] and total impulse [right axis] for the charge sizes used in the parametric study

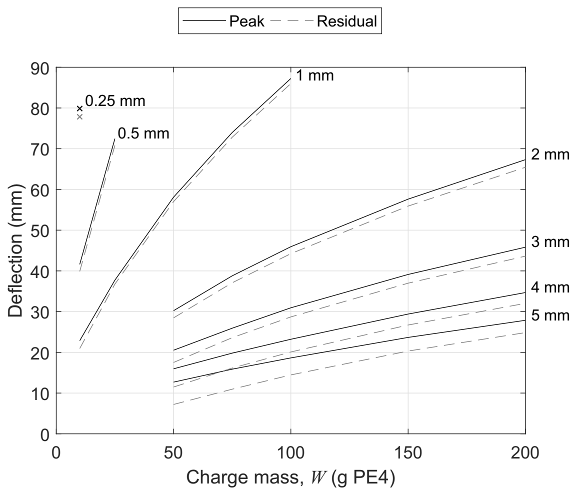

Figure 13: Peak and residual deflection against charge mass for different plate thicknesses

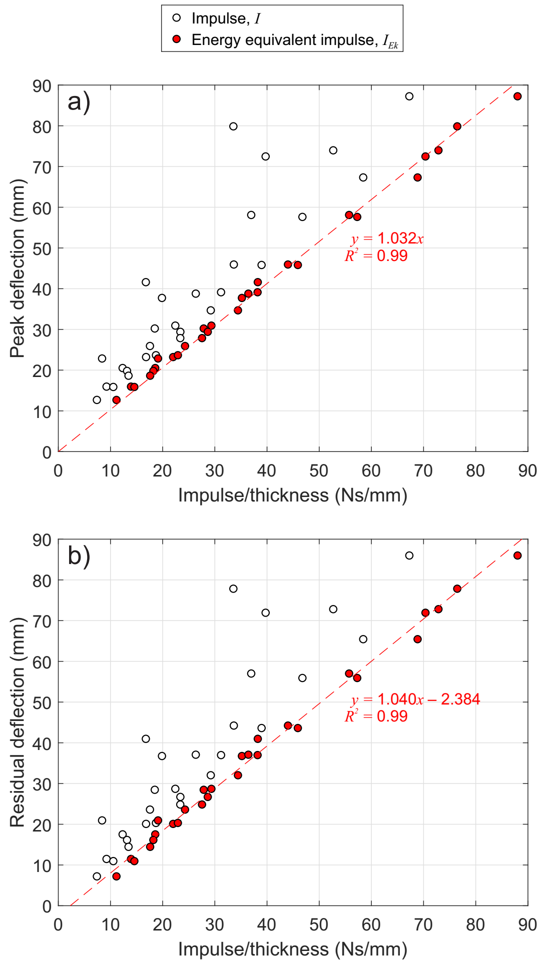

Figure 14: Deflection plotted against total impulse (I) and energy equivalent impulse ($I_{Ek} = K_i I$) per unit thickness: a) peak deflection; b) residual deflection

The results show that knowledge of the total impulse alone is not sufficient to predict the deflection of a plate subjected to a near-field blast load. Knowledge of the *spatial distribution of loading*, however, allows the total impulse to be transformed into an energy equivalent value using the impulse enhancement factor, K_i, and thus the peak and residual plate deformation can be predicted using a simple linear relationship. Whilst the parametric study in this article only considered 300 mm circular spanning Domex 355MC steel plates, the method of energy transformation has been shown to be valid for a wide range of impulsive loads and plate thicknesses. Similar relationships could be derived for different combinations of plate density, strength, and span, using the normalised relationships developed in Ref. [17].

Further interrogation of Figure 14 and Table 5 suggests that the accuracy of the linear relationship between deflection and energy equivalent impulse appears to be independent of the value of the impulse enhancement factor, i.e. the level of non-uniformity of the applied load. Take the results for a 0.5 mm plate subjected to a 25 g blast, and a 1.0 mm plate subjected to a 75 g blast as two examples. For the 0.5 mm plate the total imparted impulse is 39.7 Ns per unit thickness, the impulse enhancement factor is 1.77, and therefore the energy equivalent impulse is $39.7 \times 1.77 = 70.4$ Ns per unit thickness. The residual deflection, determined from the parametric study, is 71.9 mm. For the 1.00 mm plate, the total imparted impulse, enhancement factor, and energy equivalent impulse, are 52.7 Ns/mm, 1.38, and 72.9 Ns/mm respectively, and the peak deflection is 72.8 mm. The residual deflection profiles for both plates are shown in Figure 15.

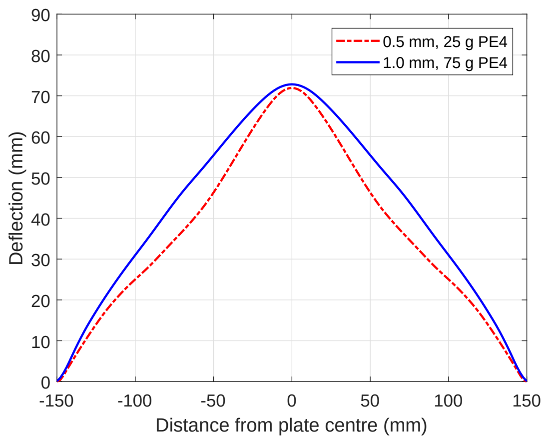

Figure 15: Residual plate deflection profiles for 0.5 mm plate subjected to a 25 g blast (39.7 Ns/mm), and 1.0 mm plate subjected to a 75 g blast (52.7 Ns/mm). Both plates have similar energy equivalent impulse per unit thickness: 70.4 Ns/mm and 72.9 Ns/mm respectively

It can be seen that both plates respond in different modes: the 1.0 mm plate deforms largely in global bending, whereas the 0.5 mm plate exhibits significant epicentral dishing on account of the loading being highly focussed in the central region. That the plates deflect by a similar amount, despite the thicker plate being subjected to 33% more impulse than the thinner plate, suggests that the energy equivalent impulse approach is insensitive to the deformation mode of the plate, and can accurately predict the peak deflection for various response modes.

6. Summary and conclusions

This article presents a study into blast loading and dynamic response of structures subjected to blast loads. Direct measurements of reflected pressure arising from the detonation of spherical and cylindrical PE4 charges [1] were used to validate LS-DYNA's MMALE capabilities, with the models showing reasonable agreement for specific impulse distribution, despite discrete pressure-time histories appearing to be in poor agreement for the cylindrical explosives.

Additional experiments conducted in [1], where dynamic plate deformations were measured using digital image correlation, were used to validate two types of LS-DYNA models: MMALE models where detonation, blast wave propagation and reflection were simulated directly and blast loads were applied to the structure through fluid-structure interaction, and Lagrangian models where previously recorded specific impulse distributions [1] were applied directly to the structure as nodal-point initial velocities. The numerical models showed excellent agreement with the experimental results, in particular the Lagrangian models which predicted peak deflections to within 1% of the experimental recordings, and ran for considerably less time than the MMALE models.

The Lagrangian models were used perform a parametric study of the deformation of plates with consistent span and material properties but varying thickness, subjected to the blast load from spheres of varying mass at the same scaled distance (i.e. the loading was scaled directly from the experimental measurements). Additionally, the energy equivalent impulse and impulse enhancement factor were derived, which can be used to account for the additional energy imparted to a plate from a non-uniform impulse load.

The results from the parametric study show that there exists a linear relationship between plate deformation and energy equivalent impulse per unit thickness. The relationship was shown to be insensitive to changes in loading distribution and deformation mode. The energy equivalent impulse method has clear applications for the development of fast-running engineering tools for the prediction of structural response to near-field blast explosions.

7. Data access statement

The data presented in this publication can be obtained on request by contacting sam.rigby@sheffield.ac.uk

Acknowledgements

The first author acknowledges the financial support from the Royal Academy of Engineering Newton Research Collaboration Programme (NCRP1617/6/212).

[1] S. E. Rigby, A. Tyas, R. J. Curry, and G. S. Langdon. Experimental measurement of specific impulse distribution and transient deformation of plates subjected to near-field explosive blasts. *Experimental Mechanics. In press. Accepted.*

[2] C. N. Kingery and G. Bulmash. Airblast parameters from TNT spherical air burst and hemispherical surface burst. Technical Report ARBRL-TR-02555, U.S Army BRL, Aberdeen Proving Ground, MD, USA, 1984.

[3] J. M. Biggs. *Introduction to Structural Dynamics*. McGraw-Hill, New York, NY, USA, 1964.

[4] S. E. Rigby, A. Tyas, and T. Bennett. Single degree of freedom response of finite targets subjected to blast loading – the influence of clearing. *Engineering Structures*, 45:396–404, 2012.

[5] S.E. Rigby, A. Tyas, S. D. Fay, S. D. Clarke, and J. A. Warren. Validation of semi-empirical blast pressure predictions for far field explosions – is there inherent variability in blast wave parameters? In *6th International Conference on Protection of Structures Against Hazards (PSH14), Tianjin, China*, 2014.

[6] T. Børvik, A. G. Hanssen, M. Langseth, and L. Olovsson. Response of structures to planar blast loads – a finite element engineering approach. *Computers & Structures*, 87(9-10):507–520, 2009.

[7] M. S. Chafi, G. Karami, and M. Ziejewski. Numerical analysis of blast-induced wave propagation using FSI and ALEmulti-material formulations. *International Journal of Impact Engineering*, 36(10-11):1269–1275, 2009.

[8] A. Neuberger, S. Peles, and D. Rittel. Scaling the response of circular plates subjected to large and close-range spherical explosions. Part I: Air-blast loading. *International Journal of Impact Engineering*, 35(5):859–873, 2007.

[9] K. H. Safari, J. Zamani, S. M. R. Khalili, and S. Jalili. Experimental, theoretical, and numerical studies on the response of square plates subjected to blast loading. *The Journal of Strain Analysis for Engineering Design*, 46(8):805–816, 2011.

[10] Z. S. Tabatabaei, J. S. Volz, J. Baird, B. P. Gliha, and D. I. Keener. Experimental and numerical analyses of long carbon fiber reinforced concrete panels exposed to blast loading. *International Journal of Impact Engineering*, 57:70–80, 2013.

[11] B. Zakrisson, B. Wikman, and H. Häggblad. Numerical simulations of blast loads and structural deformation from near-field explosions in air. *International Journal of Impact Engineering*, 38(7):597–612, 2011.

[12] S. E. Rigby, A. Tyas, T. Bennett, J. A. Warren, and S. Fay. Clearing effects on plates subjected to blast loads. *Proceedings of the Institution of Civil Engineers – Engineering and Computational Mechanics*, 166(3):140–148, 2013.

[13] K. Spranghers, I. Vasilakos, D. Lecompte, H. Sol, and J. Vantomme. Full-Field Deformation Measurements of Aluminum Plates Under Free Air Blast Loading. *Experimental Mechanics*, 52(9):1371–1384, 2012.

[14] K. Spranghers, I. Vasilakos, D. Lecompte, H. Sol, and J. Vantomme. Numerical simulation and experimental validation of the dynamic response of aluminum plates under free air explosions. *International Journal of Impact Engineering*, 54:83–95, 2013.

[15] E. Borenstein and H. Benaroya. Loading and structural response models of circular plates subjected to near field explosions. *Journal of Sound and Vibration*, 332(7):1725–1753, 2013.

[16] A. Remennikov, T. Ngo, D. Mohotti, B. Uy, and M. Netherton. Experimental investigation and simplified modeling of response of steel plates subjected to close-in blast loading from spherical liquid explosive charges. *International Journal of Impact Engineering*, 101:78 – 89, 2017.

[17] G. Nurick and J. Martin. Deformation of thin plates subjected to impulsive loading – a review. Part 2: experimental studies. *International Journal of Impact Engineering*, 8:171–186, 1989.

[18] S. Chung Kim Yuen and G. N. Nurick. Experimental and numerical studies on the response of quadrangular stiffened plates. Part I: subjected to uniform blast load. *International Journal of Impact Engineering*, 31(1):55–83, 2005.

[19] G. S. Langdon, S. Chung Kim Yuen, and G. N. Nurick. Experimental and numerical studies on the response of quadrangular stiffened plates. Part II: localised blast loading. *International Journal of Impact Engineering*, 31(1):85–111, 2005.

[20] A.S. Fallah, K. Micallef, G.S. Langdon, W.C. Lee, P.T. Curtis, and L.A. Louca. Dynamic response of dyneema hb26 plates to localised blast loading. *International Journal of Impact Engineering*, 73:91 – 100, 2014.

[21] N Mehreganian, A Fallah, G Boiger, and L Louca. Response of armour steel plates to localised air blast load - a dimensional analysis. *The International Journal of Multiphysics*, 11(4):387–412, 2017.

[22] N. Mehreganian, L.A. Louca, G.S. Langdon, R.J. Curry, and N. Abdul-Karim. The response of mild steel and armour steel plates to localised air-blast loading-comparison of numerical modelling techniques. *International Journal of Impact Engineering*, 115:81 – 93, 2018.

[23] S. D. Clarke, S. D. Fay, J. A. Warren, A. Tyas, S. E. Rigby, and I. Elgy. A large scale experimental approach to the measurement of spatially and temporally localised loading from the detonation of shallow-buried explosives. *Measurement Science and Technology*, 26:015001, 2015.

[24] R. J. Curry and G. S. Langdon. Transient response of steel plates subjected to close proximity explosive detonations in air. *International Journal of Impact Engineering*, 102:102–116, 2017.

[25] M. Sutton, W. Wolters, W. Peters, W. Ranson, and S. McNeill. Determination of displacements using an improved digital correlation method. *Image and Vision Computing*, 1(3):133–139, 1983.

[26] J. O. Hallquist. *LS-DYNA Theory Manual*. Livermore Software Technology Corporation, CA, USA, 2006.

[27] B. van Leer. Towards the ultimate conservative difference scheme. IV. A new approach to numerical convection. *Journal of Computational Physics*, 23:276–299, 1977.

[28] E. L. Lee, H. C. Hornig, and J. W. Kury. Adiabatic expansion of high explosive detonation products. Technical Report TID 4500-UCRL 50422, Lawrence Radiation Laboratory, University of California, CA, USA, 1968.

[29] S. E. Rigby. *Blast Wave Clearing Effects on Finite-Sized Targets Subjected to Explosive Loads*. PhD thesis, Department of Civil & Structural Engineering, University of Sheffield, UK, 2014.

[30] D. Bogosian, M. Yokota, and S. Rigby. TNT equivalence of C-4 and PE4: A review of traditional sources and recent data. In *Proceedings of the 24th International Symposium on Military Aspects of Blast and Shock (MABS24)*, Halifax, Nova Scotia, Canada, 2016.

[31] B. M. Dobratz and P. C. Crawford. LLNL explosives handbook - properties of chemical explosives and explosive simulants. Technical Report UCRL 52997, Lawrence Livermore National Laboratory, University of California, CA, USA, 1985.

[32] D Bancroft. The velocity of longitudinal waves in cylindrical bars. *Physical Review*, 59:588–593, 1941.

[33] A. Tyas and A. J. Watson. An investigation of frequency domain dispersion correction of pressure bar signals. *International Journal of Impact Engineering*, 25(1):87–101, 2001.

[34] B. Hopkinson. *British Ordnance Board Minutes, 13565*. 1915.

[35] C. Cranz. *Lehrbuch der Basllistik*. Springer, Berlin, Germany, 1926.

[36] C. Geretto. *The Effects of Different Degrees of Confinement on the Deformation of Square Plates Subjected to Blast Loading*. PhD thesis, Department of Mechanical Engineering, University of Cape Town, South Africa, 2012.

[37] G. R. Johnson and W. H. Cook. Constitutive model and data for metals subjected to large strains, high strain rates and high temperatures. In *Proceedings of the 7th International Symposium on Ballistics*, The Hague, The Netherlands, 1983.

[38] R. Curry. *Response of plates subjected to air-blast and buried explosions*. PhD thesis, Department of Mechanical Engineering, University of Cape Town, South Africa, 2017.

[39] LSTC. Livermore software technology corporation (LSTC). http://www.lstc.com/products/ls-opt, 2017. [accessed 07/09/2017].

[40] B. Fuller et al. Effect of spatial variation of blast loading on response of plates. In *Proceedings of the First International Conference on Structural Safety Under Fire & Blast (CONFAB), Glasgow, Scotland*, 2015.